Theory and simulations of field strengths in magnetosonic shock waves in finite beta plasmas

Mieko Toida*

National Institute for Fusion Science, Toki 509-5292, Japan

Yukiharu Ohsawa

Department of Physics, Nagoya University, Nagoya 464-8602, Japan

(Dated: March 16, 2022)

Abstract

Field strengths in an oblique magnetosonic shock wave in a collisionless, finite beta plasma are studied with theory and simulations. With use of the warm, two-fluid model, the maximum values of the magnetic field, the transverse electric field, and the electric potential in a shock wave are analytically obtained as functions of the shock speed. One-dimensional, electromagnetic particle simulations are then carried out to measure the field strengths in shock waves. The theory and the simulation results are found to be consistent.

PACS numbers: 52.35.Bj, 52.35.Mw, 52.35.Sb, 52.35.Tc

*Electronic address: toida.mieko@nifs.ac.jp

I. INTRODUCTION

In the analysis of particle acceleration in plasmas [1–4], information about electric and magnetic fields is essential. In a magnetosonic shock wave [4–6], proton reflection is mainly caused by the electric potential, and we can estimate the number of reflected protons using the magnitude of the electric potential ϕ [7–13]. Also, as a function ϕ, we can express the ultrarelativistic energy of electrons accelerated by an oblique shock wave [14]. On the other hand, the transverse electric field can give rise to heavy-ion acceleration in a multi-ion species plasma with protons being the main ion constituent [15]. If we have a theory that gives these field values in a shock wave as functions of the shock speed, which can be measured even from a distance, it will enable us to quantitatively discuss particle motions in shock waves in laboratory and space plasmas.

Sagdeev suggested [5, 6] that collisionless magnetosonic shock waves have profiles with damped wave trains, which is qualitatively consistent with simulation results [4]. However, since we do not know analytic solutions for large-amplitude shock waves, we cannot quantitatively predict field values in shock waves even if their propagation speeds are given. It is in contrast to small-amplitude solitary waves: We know their analytic solutions and thus can predict their field values at any point and time if their propagation speeds are given [4, 16, 17].

In 2003, using a relativistic, cold, two-fluid model, Miyahara *et al.* theoretically obtained the maximum field values in a magnetosonic shock wave propagating obliquely to an external magnetic field [18]. The theory gave the maximum values of the magnetic field, the transverse electric field, and the electric potential as functions of the shock speed. In addition, carrying out relativistic particle simulations, they made precise measurements of the field strengths in shock waves, confirming that the simulation results were consistent with the theory. These studies were, however, restricted to low beta plasmas, where beta is the ratio of the plasma to magnetic pressures. The plasma pressure was ignored in the theory, and the beta values were much less than unity in the simulations. In 2018, with use of a nonrelativistic, warm, two-fluid model, the theory was extended to finite beta plasmas. This theory could not give the maximum field values as functions of the shock speed, but showed relations among the maximum field values in a shock wave [19].

In this paper, we further develop the finite beta theory so that we can express the maxi-

mum field values as functions of the shock speed. Moreover, we perform particle simulations for shock waves and compare the theory and the simulation results. In Sec. II, we first mention the basic features of field profiles in shock waves that we have recognized from past theoretical and computational studies [4–6]. Next, based on the nonrelativistic, warm, two-fluid model, we analytically obtain the maximum values of the magnetic field, the electric potential, and the transverse electric field in a shock wave as functions of the shock speed by using the relations among field strengths given by Ref. [19]; a short preliminary report on this new theory was published in Ref. [20]. In the final step of the analysis, we present two distinct models to complete the calculation. Although the viewpoints of the two models are contrasting, they lead to quantitatively similar results. In Sec. III, we test the theory with particle simulations. We carry out one-dimensional, relativistic, electromagnetic particle simulations on shock waves and measure the maximum field strengths in these waves. The simulation results are found to be consistent with the theory. Section IV gives a summary of our work.

II. THEORETICAL ANALYSIS

In Sec. II, we obtain analytic expressions for the maximum values of electric and magnetic fields in a magnetosonic shock wave. To do this, we adopt the nonrelativistic, warm, two-fluid model in which the equations for the number density n, velocity $\boldsymbol{v}$, and pressure p are, respectively, given as

$$\frac{\partial n_j}{\partial t} + \nabla \cdot (n_j \boldsymbol{v}_j) = 0, \tag{1}$$

$$n_j m_j \left(\frac{\partial}{\partial t} + (\boldsymbol{v}_j \cdot \nabla) \right) \boldsymbol{v}_j = n_j q_j \boldsymbol{E} + \frac{n_j q_j}{c} \boldsymbol{v}_j \times \boldsymbol{B} - \nabla p_j, \tag{2}$$

$$\left(\frac{\partial}{\partial t} + (\boldsymbol{v}_j \cdot \nabla) \right) p_j = -\Gamma_j p_j \nabla \cdot \boldsymbol{v}_j, \tag{3}$$

where the subscript j refers to ions ($j = i$) or electrons ($j = e$); m_j is the particle mass; q_j is the particle charge, taken to be $q_i = e$ and $q_e = -e$ with e the elementary charge; c is the speed of light; and Γ_j is the specific heat ratio.

For oblique magnetosonic waves, the left-hand side of the momentum equation (2) is negligibly small for electrons. (It is not the case with perpendicular waves [5, 16, 17, 21].)

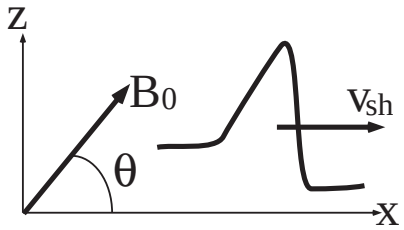

FIG. 1: Geometry of shock wave and magnetic field. The shock wave propagates in the x direction with a velocity $v_{\rm sh}$ in an external magnetic field $\boldsymbol{B}_0$ in the (x, z) plane. The angle between $\boldsymbol{B}_0$ and the x axis is denoted by θ.

We thus use the following form for the electron momentum equation:

$$\boldsymbol{E} + \frac{\boldsymbol{v}_e \times \boldsymbol{B}}{c} + \frac{\nabla p_e}{e n_e} = 0. \tag{4}$$

These equations are coupled with Maxwell equations for the magnetic field $\boldsymbol{B}$ and the electric field $\boldsymbol{E}$,

$$\frac{1}{c}\frac{\partial \boldsymbol{B}}{\partial t} = -\nabla \times \boldsymbol{E}, \tag{5}$$

$$\frac{1}{c}\frac{\partial \boldsymbol{E}}{\partial t} = \nabla \times \boldsymbol{B} - \frac{4\pi}{c}\sum_j n_j q_j \boldsymbol{v}_j. \tag{6}$$

A. Geometry, coordinate system, and basic properties of field profiles

We consider a stationary, planar, magnetosonic shock wave propagating in the x direction ($\partial/\partial y = \partial/\partial z = 0$) with a velocity $v_{\rm sh}$ in a uniform external magnetic field $\boldsymbol{B}_0$ in the $(x,\ z)$ plane, i.e.,

$$\boldsymbol{B}_0 = (B_{x0}, 0, B_{z0}) = B_0(\cos\theta, 0, \sin\theta), \tag{7}$$

as shown in Fig. 1. Here, the subscript 0 refers to equilibrium (and thus far upstream) quantities. For definiteness, we assume that $0 < \theta \leq 90^\circ$. The y axis is then perpendicular to the plane formed by the wave normal and the external magnetic field. This coordinate system is suitable for describing shock waves and will be called the shock coordinate system. In this coordinate system, the electric and the magnetic fields in the shock wave have the following distinct properties: (1) B_x is constant ($B_x = B_{x0}$), which results from the equation $\nabla \cdot \boldsymbol{B} = 0$, (2) B_z sharply rises in the front part of the shock wave and has a profile similar to those of the plasma density n, the electric potential ϕ, and the transverse electric field

E_y, and (3) B_y, E_x ($= -\partial\phi/\partial x$), and E_z are proportional to $\partial B_z/\partial x$ and hence become zero at the position $x = x_{\rm m}$ at which B_z takes its maximum value (see, for instance, Section 2.4.1 in p. 159 and Fig. 24 in p. 184 in Ref. [4]).

For $\theta \gtrsim 45^\circ$, B_z is the dominant component of the magnetic field. Hence, the magnetic-field strength B also takes its maximum value at $x = x_{\rm m}$.

Properties (2) and (3) exactly hold for small-amplitude waves such as solitary waves and wave trains governed by the Korteweg-de Vries (KdV) equation; see, for instance, Eqs. (50a) - (50g) in Ref. [10]. Furthermore, simulations show that these properties approximately hold for large-amplitude shock waves; see, for instance, Fig. 24 in [4] and Fig. 2 in Sec. III B in the present paper. It is noted, however, that in the wave frame where $\partial/\partial t = 0$, E_y and E_z are constant (independent of x), which we see from Faraday's law (5).

When observing or analyzing shock waves in space, we may not know the shock coordinate system. We briefly mention a method to obtain this coordinate system for a planar shock wave. It is obvious that if the external magnetic field $\boldsymbol{B}_0$ and the direction of the shock propagation are given, we can readily determine the shock coordinate system. Also, even if $\boldsymbol{B}_0$ is not given, we can find the shock coordinate system provided that we know the direction of the shock propagation and have observational data $\boldsymbol{B}(x', y', z')$. Here, (x', y', z') is a coordinate system that the observer is using, and in general it will not coincide with the shock coordinate system. Even if we do not know $\boldsymbol{B}_0$, we can decide the x axis; it is along the direction of the wave propagation. As suggested by properties (1) through (3), this axis plays an important role in the analysis of shock waves. Indeed, $\boldsymbol{B}$ depends only on x (and t) in a planar shock wave. In addition, B_x is constant along the x axis [property (1)], and is given as $B_{x0} = \boldsymbol{B} \cdot \boldsymbol{e}_x$, where $\boldsymbol{e}_x$ is the unit vector parallel to the x axis. From the properties (2) and (3), then, we see that the magnetic field $\boldsymbol{B}(x_{\rm m}) - [\boldsymbol{B}(x_{\rm m}) \cdot \boldsymbol{e}_x]\boldsymbol{e}_x$ points in the z direction. Since we now know the x and the z axes, we can determine the y axis in the direction perpendicular to these two axes. In this way we can find the shock coordinate system (x, y, z) from the direction of the shock propagation and a data set for $\boldsymbol{B}(x', y', z')$.

B. Maximum value of B_z

We now calculate the maximum field values in a collisionless, oblique magnetosonic shock wave in a finite beta plasma. Extending the theories for large-amplitude shock waves [18, 19],

we obtain the maximum values of B_z, E_y, and ϕ as functions of the shock propagation speed $v_{\rm sh}$ (> 0).

In the wave frame where the time derivatives are zero, $\partial/\partial t = 0$, the continuity equation (1) gives

$$n_{{\rm w}j} v_{{\rm w}jx} = -n_{{\rm w}j0} v_{\rm sh}, \tag{8}$$

where the subscript w refers to quantities in the wave frame. Equation (8) shows that $v_{{\rm w}jx}$ becomes small in magnitude at $x = x_{\rm m}$ compared with the upstream speed,

$$|v_{{\rm w}jx}(x_{\rm m})| \ll v_{\rm sh}, \tag{9}$$

because $n_{{\rm w}j}$ takes its maximum value at this point and the shock amplitude is large, $n_{{\rm w}j}(x_{\rm m}) \gg n_{{\rm w}j0}$.

To calculate the maximum field values, we rewrite the x component of the momentum equation (2) as

$$\sum_j m_j n_{{\rm w}j} v_{{\rm w}jx} \frac{dv_{{\rm w}jx}}{dx} = \sum_j q_j n_{{\rm w}j} \left(E_{{\rm w}x} + \frac{v_{{\rm w}jy}}{c} B_{{\rm w}z} - \frac{v_{{\rm w}jz}}{c} B_{{\rm w}y} \right) - \sum_j \frac{dp_{{\rm w}j}}{dx}, \tag{10}$$

where $\sum_j$ indicates summation over particle species. We simplify Eq. (10) using several approximations. Since the frequency range of the magnetosonic wave under consideration is low, we assume charge neutrality [4–6, 10, 16, 17], $n_{\rm w} = n_{{\rm w}i} \simeq n_{{\rm w}e}$, Hence, it follows from the continuity equation (1) that $v_{{\rm w}x} = v_{{\rm w}ix} \simeq v_{{\rm w}ex}$. Furthermore, we ignore the electron term on the left-hand side of Eq. (10) because m_e is small. Then, combining Eqs. (6), (8), (10), and Gauss's law, we obtain the following equation:

$$\frac{B_{{\rm w}y}^2 + B_{{\rm w}z}^2 - B_{{\rm w}z0}^2 - E_{{\rm w}x}^2}{8\pi} = m_i n_{{\rm w}0} v_{\rm sh} (v_{\rm sh} + v_{{\rm w}ix}) - \sum_j (p_{{\rm w}j} - p_{{\rm w}j0}). \tag{11}$$

On account of the relation (9) and the wave properties mentioned in Sec. II A, i.e., $B_{{\rm w}y}$ and $E_{{\rm w}x}$ are nearly zero at $x_{\rm m}$, we can ignore $B_{{\rm w}y}^2$, $E_{{\rm w}x}^2$, and $v_{{\rm w}ix}$ near the point $x_{\rm m}$ in Eq. (11). We thus have the equation between $B_{{\rm w}z{\rm m}}$ and $p_{{\rm w}j{\rm m}}$ in the wave frame [19]. Since $v_{{\rm w}ix}$ is negative [$|v_{{\rm w}ix}|$ is much smaller than $v_{\rm sh}$ but finite], the omission of $v_{{\rm w}ix}$ from Eq. (11) makes $B_{{\rm w}z}^2$ slightly greater; i.e., this approximation can slightly overestimate the value of $B_{{\rm w}z}$.

Once $B_{{\rm w}z{\rm m}}$ is given, we can obtain the equation for $B_{z{\rm m}}$ in the laboratory frame. It is because, since the present theory is non-relativistic (in particular, since $v_{\rm sh} \ll c$), we have the relations $\boldsymbol{B}_{\rm w} = \boldsymbol{B}$, $p_{{\rm w}j} = p_j$, and $n_{\rm w} = n$. We note that the relativistic theory also

shows that $B_{\mathrm{w}zm} \simeq B_{z\mathrm{m}}$ as long as $v_{\mathrm{sh}} \ll c$, which is proved in Appendix A. Hence, the equation between $B_{\mathrm{w}zm}$ and $p_{\mathrm{w}j\mathrm{m}}$ has the same form as the equation between $B_{z\mathrm{m}}$ and $p_{j\mathrm{m}}$.

We thus find the equation for $B_{z\mathrm{m}}$ in the laboratory frame as

$$\frac{B_{z\mathrm{m}}}{B_{z0}} = \left(1 + \frac{2v_{\mathrm{sh}}^2}{v_{\mathrm{A}}^2 \sin^2\theta} - \frac{\sum_j (p_{j\mathrm{m}} - p_{j0})}{B_{z0}^2/(8\pi)}\right)^{1/2}, \tag{12}$$

where v_{A} is the Alfvén speed,

$$v_{\mathrm{A}} = \frac{B_0}{(4\pi n_{i0} m_i)^{1/2}}. \tag{13}$$

If we omit the pressure terms in Eq. (12), we have the low beta theory in Ref. [18]. As can be seen from Eq. (12), the plasma pressure acts to suppress the increase in B_z. For later use, we rewrite the pressure terms in Eq. (12) as

$$\frac{\sum_j (p_{j\mathrm{m}} - p_{j0})}{B_{z0}^2/(8\pi)} = \frac{2}{v_{\mathrm{A}}^2 \sin^2\theta}\left[v_{Ti}^2\left(\frac{p_{i\mathrm{m}}}{p_{i0}} - 1\right) + \frac{m_e}{m_i} v_{Te}^2\left(\frac{p_{e\mathrm{m}}}{p_{e0}} - 1\right)\right], \tag{14}$$

where v_{Ti} and v_{Te} are, respectively, the ion and the electron thermal velocities, $v_{Tj} = (T_j/m_j)^{1/2}$ with T_j the temperature.

Next, we eliminate the pressure terms from Eq. (12) so that we can express $B_{z\mathrm{m}}/B_{z0}$ with v_{sh}, θ, and equilibrium quantities such as v_{A}. We do this in two distinct ways below in Sec. II B 1 and in Sec. II B 2.

1. *Extrapolation of a relation in small-amplitude theory*

To this point, we have done calculations under the assumption that the shock amplitude is large, such that $n_{j\mathrm{m}} \gg n_{j0}$. Here in Sec. II B 1, however, we use an equation that was obtained in a perturbation theory.

According to the theory in Ref. [10], which derived the KdV equation for nonlinear magnetosonic waves in finite beta plasmas, we can express the quantity $[(p_{j\mathrm{m}}/p_{j0}) - 1]$ in terms of $B_{z\mathrm{m}}$ as

$$\frac{p_{j\mathrm{m}}}{p_{j0}} - 1 = \frac{\Gamma_j v_{\mathrm{A}}^2 \sin\theta}{\left(v_{p0}^2 - c_s^2\right)} \frac{(B_{z\mathrm{m}} - B_{z0})}{B_0}, \tag{15}$$

where c_s is the sound speed,

$$c_s = \left(\frac{n_{i0}\Gamma_i T_{i0} + n_{e0}\Gamma_e T_{e0}}{n_{i0} m_i + n_{e0} m_e}\right)^{1/2}, \tag{16}$$

and v_{p0} is the speed of the linear magnetosonic wave in the long-wavelength limit,

$$v_{p0}^2 = (1/2)\left\{(v_{\rm A}^2 + c_s^2) + \left[(v_{\rm A}^2 + c_s^2)^2 - 4v_{\rm A}^2 c_s^2 \cos^2\theta\right]^{1/2}\right\}. \tag{17}$$

Here, for simplicity, we take the specific heat ratios to be $\Gamma_i = \Gamma_e = 1$. Extrapolating Eq. (15) to large-amplitude waves, we can put Eq. (14) in the form

$$\frac{\sum_j (p_{j\rm m} - p_{j0})}{B_{z0}^2/(8\pi)} = \frac{2c_s^2}{v_{p0}^2 - c_s^2}\left(\frac{B_{z\rm m}}{B_{z0}} - 1\right). \tag{18}$$

Substituting Eq. (18) in Eq. (12) yields the equation for $B_{z\rm m}/B_{z0}$ as

$$\left(\frac{B_{z\rm m}}{B_{z0}}\right)^2 + \frac{2c_s^2}{v_{p0}^2 - c_s^2}\left(\frac{B_{z\rm m}}{B_{z0}}\right) - \left(1 + \frac{2v_{\rm sh}^2}{v_{\rm A}^2\sin^2\theta} + \frac{2c_s^2}{v_{p0}^2 - c_s^2}\right) = 0, \tag{19}$$

from which we find $B_{z\rm m}/B_{z0}$ as a function of $v_{\rm sh}$, $v_{\rm A}$, c_s, and θ,

$$\left(\frac{B_{z\rm m}}{B_{z0}}\right) = -\frac{c_s^2}{v_{p0}^2 - c_s^2} \pm \left[\left(\frac{c_s^2}{v_{p0}^2 - c_s^2}\right)^2 + 1 + \frac{2v_{\rm sh}^2}{v_{\rm A}^2\sin^2\theta} + \frac{2c_s^2}{v_{p0}^2 - c_s^2}\right]^{1/2}. \tag{20}$$

Since we expect positive values for $B_{z\rm m}/B_{z0}$, we take the upper (plus) sign here.

2. Heuristic, large-amplitude theory

We now take another different approach to obtain the maximum value of B_z. In Sec. II B 1, we have extrapolated Eq. (15) derived from a perturbation theory to large-amplitude waves. Here, instead of adopting Eq. (15), we make use of one property of large-amplitude waves: In large-amplitude magnetosonic shock waves with $\theta \gtrsim 45°$, B_z becomes the dominant component of the magnetic field such that $B_{z\rm m} \gg B_{x0}$ even if $B_{z0} \sim B_{x0}$ [4]. In other words, as the amplitude increases, shock properties become closer to those of perpendicular shock waves.

We therefore use the following relation:

$$\frac{B_{z\rm m}}{B_{z0}} \simeq \frac{n_{j\rm m}}{n_{j0}}. \tag{21}$$

We can find this approximate form from the equation

$$\frac{\partial B_z}{\partial t} = \frac{\partial}{\partial x}(v_{ez}B_{x0} - v_{ex}B_z), \tag{22}$$

which follows from the y component of Eq. (4) and the z component of Eq. (5). As mentioned above, B_z becomes much larger than B_{x0} in a large-amplitude shock wave; consequently, the

field profiles become closer to those in a quasi-perpendicular shock wave. Furthermore, Eq. (9), which is the equation in the wave frame, indicates that $v_{ex}(x_{\rm m})$ is comparable to $v_{\rm sh}$ in the laboratory frame. Besides, as θ approaches 90°, B_z increases and v_{ez} decreases [10]. For these reasons, we can ignore the term $v_{ez}B_{x0}$ in Eq. (22) compared with the term $v_{ex}B_z$ for large-amplitude shock waves with $\theta \gtrsim 45°$. Equation (22) can thus be approximated as

$$\frac{\partial B_z}{\partial t} + \frac{\partial}{\partial x}(B_z v_{ex}) \simeq 0. \tag{23}$$

Equation (23) is an exact relation in perpendicular shock waves, in which $B_{x0} = 0$ and $v_{ez} = 0$. Comparison of Eqs. (1) and (23) shows that the equation for n_e and that for B_z have the same form, which leads to Eq. (21).

Then, noting the relation $p_j = n_j T_j$, we have

$$\frac{p_{j\rm m}}{p_{j0}} \simeq \frac{B_{z\rm m}}{B_{z0}}, \tag{24}$$

where we have assumed that the change in the temperature is small, i.e., the plasma is supposed to be isothermal. [Particle acceleration and instabilities can raise plasma temperatures in the downstream region [4–6]. However, these kinetic effects are not included in Eq. (3) and thus are out of the scope of the present theory.]

Substitution of Eq. (24) in Eq. (12) yields the equation for $B_{z\rm m}/B_{z0}$ as

$$\left(\frac{B_{z\rm m}}{B_{z0}}\right)^2 + \frac{2c_s^2}{v_{\rm A}^2 \sin^2\theta}\left(\frac{B_{z\rm m}}{B_{z0}}\right) - \left(1 + \frac{2(v_{\rm sh}^2 + c_s^2)}{v_{\rm A}^2 \sin^2\theta}\right) = 0. \tag{25}$$

We thus obtain $B_{z\rm m}/B_{z0}$ as

$$\left(\frac{B_{z\rm m}}{B_{z0}}\right) = -\frac{c_s^2}{v_{\rm A}^2 \sin^2\theta} \pm \left[\left(\frac{c_s^2}{v_{\rm A}^2 \sin^2\theta}\right)^2 + 1 + \frac{2(v_{\rm sh}^2 + c_s^2)}{v_{\rm A}^2 \sin^2\theta}\right]^{1/2}, \tag{26}$$

in which we take the upper (plus) sign.

Interestingly, although the method of obtaining the relation between $p_{j\rm m}$ and $B_{z\rm m}$, Eq. (15), in Sec. II B 1 and the method of obtaining Eq. (24) in Sec. II B 2 are contrasting, their final results, Eqs. (20) and (26), are quite similar. If we replace the term $(v_{p0}^2 - c_s^2)$ in Eq. (20) by $v_{\rm A}^2 \sin^2\theta$, Eq. (20) becomes identical to Eq. (26). We also note that in the range of angles $45° \lesssim \theta < 90°$, for which our approximations are valid, $(v_{p0}^2 - c_s^2)$ is greater than $v_{\rm A}^2 \sin^2\theta$ and approaches $v_{\rm A}^2 \sin^2\theta$ as θ goes to 90°. Hence, at 90°, $(v_{p0}^2 - c_s^2)$ is equal to $v_{\rm A}^2 \sin^2\theta$, and Eqs. (20) and (26) are identical.

C. E_{ym} and ϕ_m

Using B_{zm}, we can show the maximum values of the transverse electric field E_y and the electric potential ϕ formed in the shock wave. By virtue of Faraday's law (5), we find E_{ym} as

$$\frac{E_{ym}}{B_{z0}} = \frac{v_{sh}}{c}\left(\frac{B_{zm}}{B_{z0}} - 1\right). \tag{27}$$

Moreover, after lengthy calculations outlined in Appendix B, we find ϕ_m as [18, 19]

$$e\phi_m = e\phi_B + e\phi_p, \tag{28}$$

where

$$e\phi_B = m_i v_A^2 \left(\sin^2\theta + \sin\theta\cos^2\theta\right)\left(\frac{B_{zm}}{B_{z0}} - 1\right), \tag{29}$$

and

$$e\phi_p = \int \frac{1}{n_e}\frac{\partial p_e}{\partial x}dx. \tag{30}$$

The electric potential ϕ_p given by Eq. (30) is due to the electron thermal pressure p_e and would be of the order of the electron temperature T_e; if T_e is constant, Eq. (30) gives $e\phi_p = T_e \ln(n_{em}/n_{e0})$. Substituting Eq. (21) in this equation gives

$$e\phi_p = T_e \ln\left(\frac{B_{zm}}{B_{z0}}\right). \tag{31}$$

Appendix B calculates the potential under the assumption that $\theta \gtrsim 45°$. For $\theta \lesssim 45°$, the approximations in the calculations would not be accurate enough [18]. It is noted also that, aside from the accuracy, we should restrict ourselves to the range $\theta \gtrsim 45°$. As the propagation angle θ becomes smaller than this range, the field profiles begin to look quite different from those described in Sec. II A. In front of the main pulse region of a shock wave, we have large-amplitude wave trains propagating faster than the shock wave; see, for instance, Fig. 5 in Ref. [18]. The generation of such wave trains would be due to the positive dispersion [4–6].

In Sec. III, we examine the validity of our analytical results, Eqs. (20) and Eqs. (26) through (31), with particle simulations. We do this because the present theory is based on several assumptions and approximations. For instance, the shock wave was assumed to be stationary; thus, the time derivatives in the field equations (1) - (6) were set to be zero, $\partial/\partial t = 0$, in the wave frame. However, shock waves are not perfectly stationary. They

always have some fluctuations even in the absence of instabilities. In addition, the theory is based on the fluid model and does not take into account kinetic effects such as proton reflection, which can give rise to amplitude oscillations [26]. When a shock wave reflects a bunch of protons forward at the shock front, the shock wave temporarily loses some energy and the maximum field values decrease. As the reflected protons return to and enter the shock wave, however, the field profiles recover and a new reflection process begins again; in this way, $B_{z\mathrm{m}}(t)$ and the other maximum field values oscillate with time t. The period of the amplitude oscillation [26] is of the order of half of the proton gyroperiod, $\sim \pi/\Omega_i$. Particle simulations enable us to study shock phenomena including these effects in a self-consistent manner.

III. NUMERICAL STUDY OF FIELD STRENGTHS

In 1985, Ohsawa [25] studied shock waves and particle acceleration with particle simulations, using a two-dimensional, fully kinetic, particle simulation code. That code was supposed to deal with current-driven instabilities that might grow in the shock wave. However, while those simulations showed strong proton acceleration in the shock wave, noticeable instabilities were not observed. Then, in 1987, Tokar *et al.* [11] carried out simulations with a code similar to that in Ref. [25]; i.e., a two-dimensional, fully kinetic code. They reported that "shock parameters are chosen to maximize the growth rates of the current driven ion acoustic instability in the shock" and that "However, the amount of resistive electron heating was small and ion reflection provides the major source of dissipation." This conclusion is basically in accord with that of Ref. [25].

These results indicate that it is worth while to study planar shock waves with one-dimensional codes, even though they cannot treat current-driven instabilities. Indeed, by use of one-dimensional codes, various shock phenomena have been found and analyzed [4].

A. Simulation model and parameters

We use a one-dimensional (one spatial coordinate and three velocity components), relativistic, electromagnetic, particle simulation code with full ion and electron dynamics [22, 23] to study the evolution of shock waves and measure the field strengths in these waves. The

code adopts the bounded plasma model [24], in which the plasma is isolated with vacuum outside. The initial plasma density near the left boundary of the plasma region is set to be high compared with the background density. The particles in the high density region initially have, on average, a finite velocity $\boldsymbol{v}_0$, which is perpendicular to $\boldsymbol{B}_0$ and is in the (x, z) plane with its x component being positive; thus these particles act as a piston to create a shock wave by pushing neighboring particles. More detailed descriptions related to this shock simulation model can be found in Refs. [14, 25].

The simulation parameters are as follows: The total grid size is $L_x = 2^{14}\Delta_{\rm g}$, where $\Delta_{\rm g}$ is the grid spacing. The left and the right boundaries of the plasma region are, respectively, $x_{\rm L} = 800\Delta_{\rm g}$ and $x_{\rm R} = 15584\Delta_{\rm g}$. The width of the initial high-density region is $600\Delta_{\rm g}$, with its plasma density three times as high as the background density. The numbers of simulation particles are $N_i = N_e \simeq 6.29\times10^6$; the ion-to-electron mass ratio is $m_i/m_e = 400$; and the speed of light is $c/(\omega_{pe}\Delta_{\rm g}) = 10.0$, where ω_{pe} is the electron plasma frequency, $\omega_{pe} = (4\pi ne^2/m_e)^{1/2}$ with n being the electron density averaged over the plasma region. We take the ratio of the electron gyrofrequency $|\Omega_e|$ $[= eB_0/(m_e c)]$ to the electron plasma frequency to be $|\Omega_e|/\omega_{pe} = 0.3$, which is 1/10 of the value $|\Omega_e|/\omega_{pe} = 3$ used in the simulations for low beta plasmas in Ref. [18]. With these parameters, the Alfvén speed is determined as $v_{\rm A}/(\omega_{pe}\Delta_{\rm g}) = (m_e/m_i)^{1/2}[c/(\omega_{pe}\Delta_{\rm g})](|\Omega_e|/\omega_{pe}) = 0.15$. The ion thermal velocity is fixed to be $v_{Ti}/(\omega_{pe}\Delta_{\rm g}) = 0.005$.

We change the beta value by changing the electron thermal velocity in the range from $v_{Te}/(\omega_{pe}\Delta_{\rm g}) = 0.5$ to 2.0, with the other parameters kept unchanged. The beta value, $(n_iT_i + n_eT_e)/(B_0^2/8\pi) = 2(m_e/m_i)v_{Te}^2/v_{\rm A}^2 + 2v_{Ti}^2/v_{\rm A}^2$, is given as $\beta = 0.06$ for $v_{Te}/(\omega_{pe}\Delta_{\rm g}) = 0.5$ and $\beta = 0.89$ for $v_{Te}/(\omega_{pe}\Delta_{\rm g}) = 2.0$. For these v_{Ti} and v_{Te}, the ion temperature is much lower than the electron temperatures. As a result, Γ_i has little effect on Eqs. (20) and (26); we see that the term $n_{i0}\Gamma_i T_{i0}$ can be ignored in the equation for c_s, Eq. (16), if $T_i \ll T_e$.

B. Simulation results

Figure 2 shows snapshots of field profiles of a shock wave with $\theta = 75^\circ$ in a plasma with $v_{Te}/(\omega_{pe}\Delta_{\rm g}) = 0.5$; thus $\beta = 0.06$ and $v_{p0}/(\omega_{pe}\Delta_{\rm g}) = 0.152$. The shock speed is $v_{\rm sh} = 2.90v_{p0}$, which is sufficiently lower than the speed of light, $v_{\rm sh}/c = 0.044$. These are the profiles in the laboratory frame where the plasma is at rest in the upstream region. The

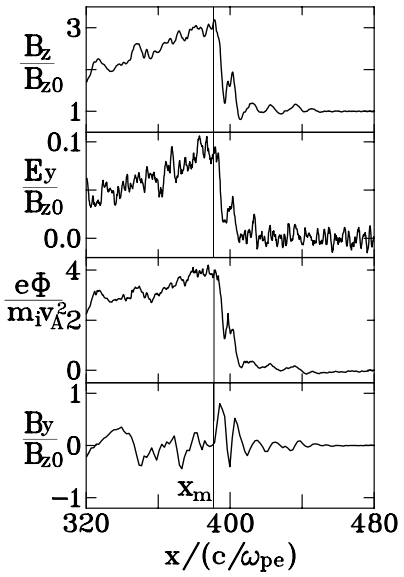

FIG. 2: Field profiles in a shock wave. The fields B_z, E_y, and ϕ have their maximum values at $x_{\rm m}/(c/\omega_{pe}) \simeq 390$ at $\omega_{pe}t = 5400$, while $B_y(x_{\rm m}) \simeq 0$. Since the values of B_y are small near $x_{\rm m}$, we have smoothed out the noises of B_y by spatial averaging.

fields are divided into two groups: E_y and ϕ as well as B_z take their maximum values near the position $x = x_{\rm m}$, while $B_y(x_{\rm m})$ is nearly zero (E_x and E_z, which are not shown here, are also nearly zero there). These features are consistent with the shock properties described in Sec. II A.

Performing such simulations, we have measured the maximum field values in various shock waves. The left panels in Fig. 3 display the maximum values of B_z, E_y, and ϕ in shock waves with $\theta = 75^\circ$ as functions of the Mach number, $v_{\rm sh}/v_{p0}$, for $v_{Te}/(\omega_{pe}\Delta_{\rm g}) = 0.5$ ($\beta = 0.06$), while the right panels are for $v_{Te}/(\omega_{pe}\Delta_{\rm g}) = 1.0$ ($\beta = 0.224$). Also, the left and the right panels in Fig. 4 show the cases with $v_{Te}/(\omega_{pe}\Delta_{\rm g}) = 1.5$ ($\beta = 0.502$) and with $v_{Te}/(\omega_{pe}\Delta_{\rm g}) = 2.0$ ($\beta = 0.891$), respectively. The closed and the open circles represent our simulation results. Take $B_{z\rm m}$ in the top panels for example; we have depicted both $B_{z\rm m}(t_{\rm lg})$ and $B_{z\rm m}(t_{\rm sm})$ for each Mach number, where $t_{\rm lg}$ and $t_{\rm sm}$ are, respectively, the times at which $B_{z\rm m}(t)$ takes its largest and smallest values in one period of the amplitude oscillation. The solid lines show our theory. For $B_{z\rm m}$, we used the theory adopting the

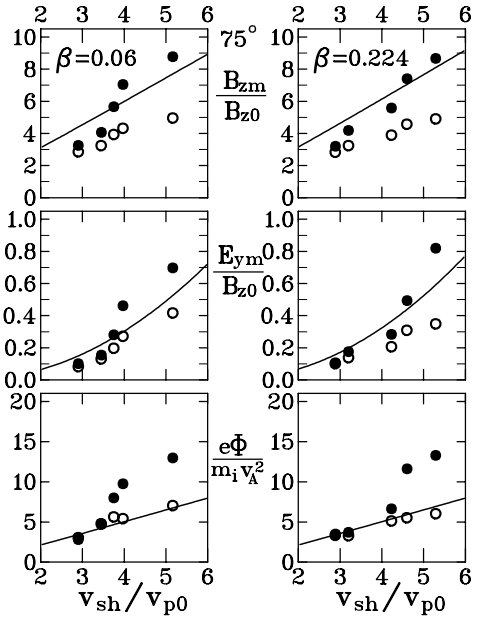

FIG. 3: Maximum field values versus Mach number $v_{\rm sh}/v_{p0}$ for $\beta = 0.06$ (left panels) and for $\beta = 0.224$ (right panels). The closed and the open circles, respectively, show the peak field values at $t = t_{\rm lg}$ and at $t = t_{\rm sm}$ observed in the simulations. The solid lines show the theory.

heuristic, large-amplitude approximation, Eq. (26). The theory containing the extrapolation for $B_{z\rm m}$, Eq. (20), is not depicted here because Eqs. (20) and (26) give quite close values; even for the high-beta case, $v_{Te}/(\omega_{pe}\Delta_{\rm g}) = 2.0$, their difference is less than 1 percent for our simulation parameters. For $E_{y\rm m}$ and $\phi_{\rm m}$, Eqs. (27)-(29) and (31) were used. The magnitude of $\phi_{\rm p}$, Eq. (31), is considerably smaller than $\phi_{\rm B}$, Eq. (29); approximately 1 percent for the case $v_{Te}/(\omega_{pe}\Delta_{\rm g}) = 0.5$ and 15 percent for $v_{Te}/(\omega_{pe}\Delta_{\rm g}) = 2.0$.

We first look at the magnetic field $B_{z\rm m}$ depicted in the top panels in Figs. 3 and 4. The theory lines are closer to the closed circles representing $B_{z\rm m}(t_{\rm lg})$ than to the open circles representing $B_{z\rm m}(t_{\rm sm})$. It is understandable because in the large-amplitude phase ($t \simeq t_{\rm lg}$) in the amplitude oscillation, $B_z(x)$ has a dominant pulse rising sharply in the front part as shown in Fig. 2, which was supposed in our theory, while in the small-amplitude phase ($t \simeq t_{\rm sm}$), $B_z(x)$ has several pulses with similar peak values. In Appendix C, we show an example of such field profiles in the small-amplitude phase and explain how we measured

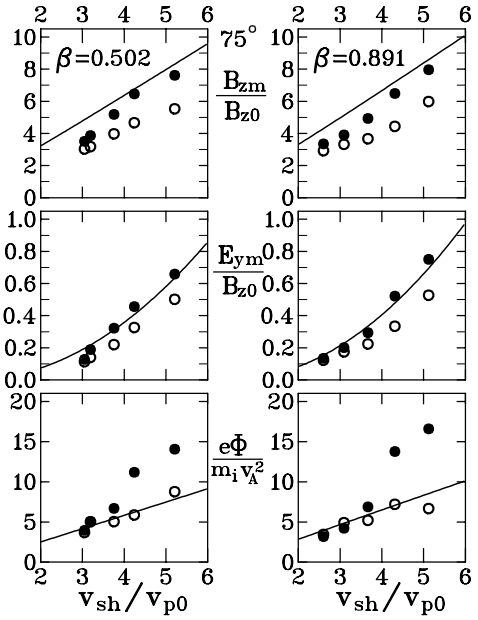

FIG. 4: Maximum field values versus Mach number $v_{\rm sh}/v_{p0}$ for $\beta = 0.502$ (left panels) and for $\beta = 0.891$ (right panels). The closed and the open circles, respectively, show the peak field values at $t = t_{\rm lg}$ and at $t = t_{\rm sm}$ observed in the simulations. The solid lines show the theory.

those field values. We mainly compare the theory with the data in the large-amplitude phase (closed circles) below.

The theory and the simulations give the same order of magnitude in both the lower beta plasmas shown in Fig. 3 and the higher beta plasmas in Fig. 4. The differences between the theory lines and the simulation values (closed circles) are within 30 percent.

For Mach numbers $v_{\rm sh}/v_{p0} \lesssim 4$, the theoretical values of $B_{z\rm m}$ are slightly greater than the observed ones in Figs. 3 and 4. This is consistent with the statement below Eq. (11) that the theory would slightly overestimate the value of $B_{z\rm m}$ because of the omission of $v_{{\rm w}ix}$ from Eq. (11).

We also find that the simulation values increase with increasing Mach number slightly more than the theoretical ones do. This phenomenon is believed to arise from the amplitude oscillation. As the Mach number goes up, the magnitude of the amplitude oscillation, which may be given as $B_{z\rm m}(t_{\rm lg}) - B_{z\rm m}(t_{\rm sm})$, grows larger, which pushes up the field values in the

large-amplitude phase ($t \simeq t_{\rm lg}$).

The theory and the simulations for the transverse electric field $E_{y\rm m}$ are depicted in the second panels in Figs. 3 and 4. As expected from the straightforward derivation of Eq. (27), $E_{y\rm m}$ behaves similarly to $B_{z\rm m}$.

The electric potential shown in the bottom panels in Figs. 3 and 4 exhibits behavior qualitatively similar to that of $B_{z\rm m}$ and $E_{y\rm m}$. However, the differences between the theoretical and the simulation values become fairly large in high Mach numbers. Although the differences between the theory and the simulation values are less than 20 percent for Mach numbers $v_{\rm sh}/v_{p0} \lesssim 4$, the simulation values can be twice as large as the theoretical ones for $v_{\rm sh}/v_{p0} \gtrsim 4$.

In the second data from the left ($v_{\rm sh}/v_{p0} = 3.09$) for $\beta = 0.89$, the closed circle is slightly under the open circle; i.e., $\phi_{\rm m}(t_{\rm lg}) < \phi_{\rm m}(t_{\rm sm})$. It can take place because we defined $t_{\rm lg}$ and $t_{\rm sm}$, respectively, as the times when $B_{z\rm m}(t)$ takes its largest and smallest values; therefore, $t_{\rm lg}$ is not necessarily the time when $\phi_{\rm m}$ takes its largest value. If the amplitude oscillation is small and thus the shock amplitude does not change much in time, $\phi_{\rm m}(t_{\rm lg})$ can occasionally become smaller than $\phi_{\rm m}(t_{\rm sm})$ as a result of the field fluctuations unrelated to the amplitude oscillation.

Although the phenomenon that the simulation values increase more steeply with the Mach number than the theory was also seen in $B_{z\rm m}$ and $E_{y\rm m}$, this tendency is enhanced in the electric potential; that is, the effect of the amplitude oscillation is more significant in the electric potential. It occurs because ϕ is determined by and thus sensitive to the spatial distribution of charged particles. The change in the distribution of charged particles arising from the proton reflection at the shock front directly affects the profile and the magnitude of ϕ [26].

We should note the possibility, however, that the shock waves in our simulations might have greater amplitude oscillations than shock waves in space. The magnitude of the amplitude oscillation would depend on the scale lengths of time and space of the processes of shock formation, as well as on the Mach number. In our simulation model, a localized, high density plasma starts pushing the neighboring plasma suddenly at $t = 0$ and creates a shock wave. Obviously, the length of the high density region, which is only $60c/\omega_{pe}$, is much smaller than those in explosions in space such as solar flares and supernovae. This would enhance the nonstationarity of shock waves in our simulations.

IV. SUMMARY

We have theoretically studied the field strengths in an oblique magnetosonic shock wave in a finite beta plasma using the two-fluid model. Furthermore, we have carried out particle simulations of shock waves to test the theory.

First, by extending the previous cold plasma theory [18, 19] to the warm plasma theory, we have analytically obtained the maximum values of the magnetic field B_z, the transverse electric field E_y, and the electric potential ϕ in a shock wave in a finite beta plasma as functions of the shock speed $v_{\rm sh}$. We calculated these values in two different ways, and these two calculations gave results similar to each other.

We then examined our theory with one-dimensional, electromagnetic particle simulations. We observed the evolution of shock waves with the propagation angle $\theta = 75^\circ$ and showed the maximum field strengths in these waves as functions of the Mach number $v_{\rm sh}/v_{p0}$ for four different beta values ranging from $\beta = 0.06$ to 0.89. The simulation results are found to be consistent with the theory.

As mentioned in Sec. I, information about field strengths is essential for the investigation of particle motions. The present work enables us to estimate the field strengths in shock waves in laboratory and space plasmas with use of measured shock speeds without detailed observational data of fields in shock waves and thus will help us make quantitative analyses of particle motions in those waves.

Appendix A: Relation between $B_{\rm wzm}$ and $B_{z\rm m}$ in the relativistic theory

In the relativistic theory, B_z is related to $B_{\rm wz}$ through

$$B_z = \gamma_{\rm sh}(B_{\rm wz} + v_{\rm sh}E_{\rm wy0}/c), \tag{A1}$$

where $\gamma_{\rm sh}$ is the Lorentz factor corresponding to the shock speed, $\gamma_{\rm sh} = (1 - v_{\rm sh}^2/c^2)^{-1/2}$. Since

$$E_{\rm wy} = E_{\rm wy0} = -(v_{\rm sh}/c)B_{\rm wz0}, \tag{A2}$$

in the wave frame, the magnitude of the second term on the right-hand side of Eq. (A1) is

$$|v_{\rm sh}E_{\rm wy0}/c| \sim (v_{\rm sh}^2/c^2)B_{\rm wz0} \lesssim (v_{\rm sh}^2/c^2)B_{\rm wz}. \tag{A3}$$

Because $v_{\rm sh} \ll c$ is assumed, we can ignore the term $v_{\rm sh}E_{{\rm w}y0}/c$ compared with the term $B_{{\rm w}z}$ in Eq. (A1), which results in the relation $B_{{\rm w}z{\rm m}} \simeq B_{z{\rm m}}$. (If the terms of the order of $\sim v_{\rm sh}^2/c^2$ are ignored, $\gamma_{\rm sh}$ becomes unity.)

Similarly, from the relation

$$B_{{\rm w}z} = \gamma_{\rm sh}(B_z - v_{\rm sh}E_y/c), \tag{A4}$$

we can prove that $B_{{\rm w}z{\rm m}} \simeq B_{z{\rm m}}$. Indeed, with the help of the equation for the transverse electric field $E_{y{\rm m}}$, i.e., Eq. (27), we can estimate the magnitude of the second term on the right-hand side of Eq. (A4) as $v_{\rm sh}E_y/c \sim (v_{\rm sh}^2/c^2)B_z$, which shows that the second term is negligibly small.

Appendix B: Maximum value of electric potential

Here we outline the calculations in Ref. [19] to derive the maximum value of the electric potential. As in Sec. II, the shock wave is supposed to steadily propagate in the x direction with a speed $v_{\rm sh}$ in an external magnetic field given by Eq. (7).

If the maximum magnetic field $B_{z{\rm m}}$ is known, we can calculate the maximum electric potential as a function of $B_{z{\rm m}}$, with the help of Ampère's law (6). To estimate the currents in Eq. (6), we need fluid velocities. By virtue of Eqs. (4) and (A2), we find the x, y, and z components of the fluid electron velocity as

$$v_{{\rm we}x} = \frac{cE_{{\rm w}y0}B_{{\rm w}z}}{B_{\rm w}^2} + \frac{v_{{\rm we}\parallel}B_{{\rm w}x0}}{B_{\rm w}}, \tag{B1}$$

$$v_{{\rm we}y} = -\frac{cE_{{\rm w}x}B_{{\rm w}z}}{B_{\rm w}^2} + \frac{v_{{\rm we}\parallel}B_{{\rm w}y}}{B_{\rm w}} - \frac{cB_{{\rm w}z}}{en_{\rm we}B_{\rm w}^2}\frac{\partial p_e}{\partial x}, \tag{B2}$$

$$v_{{\rm we}z} = \frac{c(E_{{\rm w}x}B_{{\rm w}y} - E_{{\rm w}y0}B_{{\rm w}x0})}{B_{\rm w}^2} + \frac{v_{{\rm we}\parallel}B_{{\rm w}z}}{B_{\rm w}} + \frac{cB_{{\rm w}y}}{en_{\rm we}B_{\rm w}^2}\frac{\partial p_e}{\partial x}, \tag{B3}$$

where the subscript $\parallel$ indicates the component parallel to the magnetic field. The electron fluid velocity consists of the $\boldsymbol{E} \times \boldsymbol{B}$ drift, which is represented by the first terms on the right-hand side of Eqs. (B1) - (B3), the flow along the magnetic field represented by the second terms proportional to $v_{{\rm we}\parallel}$, and the diamagnetic drift represented by the third terms proportional to $\partial p_e/\partial x$.

Substituting Eq. (B2) in the y component of Eq. (6) yields

$$\frac{dB_{{\rm w}z}}{dx} = -\frac{4\pi n_{\rm wi}ev_{{\rm wi}y}}{c} + \frac{4\pi n_{\rm we}e}{c}\left(-\frac{cE_{{\rm w}x}B_{{\rm w}z}}{B_{\rm w}^2} + \frac{v_{{\rm we}\parallel}B_{{\rm w}y}}{B_{\rm w}} - \frac{cB_{{\rm w}z}}{en_{\rm we}B_{\rm w}^2}\frac{\partial p_{\rm we}}{\partial x}\right). \tag{B4}$$

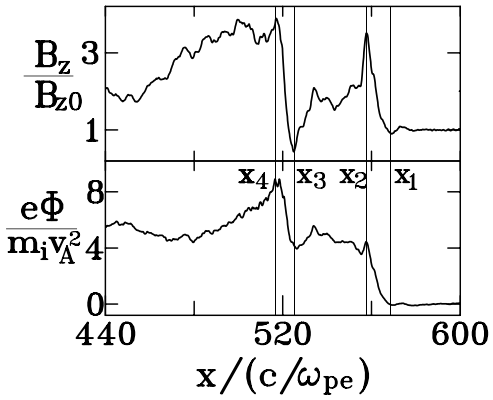

FIG. 5: Profiles of B_z and ϕ in small-amplitude phase. There are several pulses with their peak values comparable to each other, which differs from the field profiles in a large-amplitude phase shown in Fig. 2.

We eliminate the electron density $n_{\rm we}$ using Eq. (8). Then, with the help of Eqs. (A2) and (B1), we have the longitudinal electric field ($E_{{\rm w}x} = -\partial\phi_{\rm w}/\partial x$) as

$$\frac{\partial\phi_{\rm w}}{\partial x} = \left(B_{{\rm w}z0} - \frac{v_{{\rm we}\parallel}}{v_{\rm sh}}\frac{B_{{\rm w}x0}B_{\rm w}}{B_{{\rm w}z}}\right)\left(\frac{1}{4\pi n_{{\rm we}0}e}\frac{dB_{{\rm w}z}}{dx} + \frac{n_{\rm wi}v_{{\rm wi}y}}{n_{{\rm we}0}c}\right) - \frac{v_{{\rm we}\parallel}}{c}\frac{B_{{\rm w}y}B_{\rm w}}{B_{{\rm w}z}} + \frac{1}{en_{\rm we}}\frac{\partial p_{\rm we}}{\partial x}. \tag{B5}$$

By integrating Eq. (B5), we obtain, after some algebra, the electric potential, Eqs. (28) - (30) [18, 19]. The potential ϕ_p, Eq. (30), stems from the last term proportional to $\partial p_{\rm we}/\partial x$ in Eq. (B5), while $\phi_{\rm B}$ given by Eq. (29) arises from the other terms. These calculations have been made under the assumption that $\theta \gtrsim 45°$. We also note that, as in the case of B_z, since $v_{\rm sh} \ll c$, the electric potential ϕ in the laboratory frame is nearly the same as ϕ in the wave frame.

Appendix C: Field profiles in small-amplitude phase

We here discuss the field profiles in a small-amplitude phase and explain how we measured those field values.

Figure 5 displays the profiles of B_z and ϕ at $\omega_{pe}t = 5200$ in a shock wave with $v_{\rm sh}/v_{p0} = 3.76$ in a plasma with $\beta = 0.06$. This shock wave is in a small-amplitude phase at this moment.

Unlike the field profiles in the large-amplitude phase shown in Fig. 2, $B_z(x)$ has several

peaks with the same order of magnitude, with the highest peak at $x = x_4(t)$; x_4 has been $x_{\rm m}$ to this point. The peak $B_z(x_4)$ is now decreasing with time and is fading out. On the other hand, the peak $B_z(x_2)$ in the front part is growing; it will soon exceed $B_z(x_4)$ and become the highest peak. In the amplitude oscillation, such process is repeated (more detailed time variations of field profiles are shown in Ref. [26]). The amplitude oscillation can be viewed as an example of the strong stability of shock waves [27].

The electric potential in the lower panel sharply rises in two regions; in $x_1 < x < x_2$ in the front pulse and in $x_3 < x < x_4$ in the highest pulse. We recorded the jump $\phi(x_4) - \phi(x_3)$ as the magnitude of the electric potential at this moment; i.e., the other jumps such as the one in the front part, $\phi(x_2) - \phi(x_1)$, are not included in the present definition of the maximum value of the electric potential.

---

[1] C. Joshi and T. Katsouleas, Physics Today **56**, No. 6, 47 (2003).

[2] T. Tajima and J. M. Dawson, Phys. Rev. Lett. **43**, 267 (1979).

[3] W. B. Mori, C. Joshi, J. M. Dawson, D. W. Forslund, and J. M. Kindel, Phys. Rev. Lett. **69**, 1298 (1988).

[4] Y. Ohsawa, Physics Reports **536**, pp. 147-254 (2014).

[5] R. Z. Sagdeev, in *Reviews of Plasma Physics*, edited by M. A. Leontovich (Consultants Bureau, New York, 1966), Vol. 4, pp. 23-91.

[6] D. A. Tidman and N. A. Krall, *Shock Waves in Collisionless Plasmas* (John Wiley & Sons, New York, 1971).

[7] C. S. Morawetz, Phys. Fluids **4**, 988 (1961).

[8] D. Biskamp and H. Welter, Nuclear Fusion **12**, 663 (1972).

[9] D. W. Forslund, K. B. Quest, J. U. Brackbill, and K. Lee, J. Geophys. Res. **89**, A4, 2142 (1984).

[10] Y. Ohsawa, Phys. Fluids **29**, 1844 (1986).

[11] R. L. Tokar, S. P. Gary, and K. B. Quest, Phys. Fluids **30**, 2569 (1987).

[12] M. A. Lee, V. D. Shapiro, and R. Z. Sagdeev, J. Geophys. Res. **101**, A3, 4777 (1996).

[13] R. Gueroult and N. J. Fisch, Phys. Plasmas **23**, 032113 (2016).

[14] N. Bessho and Y. Ohsawa, Phys. Plasmas **6**, 3076 (1999); *ibid.* **9**, 979 (2002).

[15] M. Toida and Y. Ohsawa, Solar Physics **171**, 161 (1997).

[16] C. S. Gardner and G. K. Morikawa, Commun. Pure Appl. Math. **18**, 35 (1965).

[17] T. Kakutani, H. Ono, T. Taniuti, and C. C. Wei, J. Phys. Soc. Jpn. **24**, 1159 (1968).

[18] S. Miyahara, T. Kawashima, and Y. Ohsawa, Phys. Plasmas **10**, 98 (2003).

[19] Y. Ohsawa, Phys. Plasmas **25**, 052305 (2018).

[20] Y. Ohsawa, J. Phys. Soc. Jpn. **89**, 115003 (2020).

[21] Y. Ohsawa, Phys. Fluids **29**, 2474 (1986).

[22] P. C. Liewer, A. T. Lin, J. M. Dawson, and M. Z. Caponi, Phys. Fluids **24**, 1364 (1981).

[23] J. M. Dawson, Rev. Mod. Phys. **55**, pp. 403-448 (1983).

[24] V. K. Decyk and J. M. Dawson, J. Comput. Phys. **30**, 407 (1979).

[25] Y. Ohsawa, Phys. Fluids **28**, 2130 (1985).

[26] T. Kawashima, S. Miyahara, and Y. Ohsawa, J. Phys. Soc. Jpn. **72**, 1664 (2003).

[27] R. Gueroult, Y. Ohsawa, and N. J. Fisch, Phys. Rev. Lett. **118**, 125101 (2017).